



AMERICAN METEOROLOGICAL SOCIETY

Journal of Physical Oceanography

EARLY ONLINE RELEASE

This is a preliminary PDF of the author-produced manuscript that has been peer-reviewed and accepted for publication. Since it is being posted so soon after acceptance, it has not yet been copyedited, formatted, or processed by AMS Publications. This preliminary version of the manuscript may be downloaded, distributed, and cited, but please be aware that there will be visual differences and possibly some content differences between this version and the final published version.

The DOI for this manuscript is doi: 10.1175/JPO-D-17-0190.1

The final published version of this manuscript will replace the preliminary version at the above DOI once it is available.

If you would like to cite this EOR in a separate work, please use the following full citation:

Dosser, H., and M. Timmermans, 2017: Inferring circulation and lateral eddy fluxes in the Arctic Ocean's deep Canada Basin using an inverse method. *J. Phys. Oceanogr.* doi:10.1175/JPO-D-17-0190.1, in press.

© 2017 American Meteorological Society



1 **Inferring circulation and lateral eddy fluxes in the Arctic Ocean's**
2 **deep Canada Basin using an inverse method**

3 Hayley V. Dosser* and Mary-Louise Timmermans

4 *Yale University, New Haven, Connecticut,*

5 * *Corresponding author address:* Department of Geology and Geophysics, Yale University, New
6 Haven, Connecticut, USA.

7 E-mail: hayley.dosser@yale.edu

ABSTRACT

8 The deep waters in the Canada Basin display a complex temperature and
9 salinity structure, the evolution of which is poorly understood. The funda-
10 mental physical processes driving changes in these deep water masses are
11 investigated using an inverse method based on tracer conservation combined
12 with empirical orthogonal function analysis of repeat hydrographic measure-
13 ments between 2003 and 2015. Changes in tracer fields in the deep Canada
14 Basin are found to be dominated by along-isopycnal diffusion of water proper-
15 ties from the margins into the central basin, with advection by the large-scale
16 Beaufort Gyre circulation, as well as localized vertical mixing, playing impor-
17 tant secondary roles. In the Barents Sea Branch of the Atlantic Water Layer,
18 centered around 1200 m depth, diffusion is shown to be nearly twice as impor-
19 tant as advection to lateral transport. Along-isopycnal diffusivity is estimated
20 to be $\sim 300\text{-}600 \text{ m}^2 \text{ s}^{-1}$. Large-scale circulation patterns and lateral advective
21 velocities associated with the anticyclonic Beaufort Gyre are inferred, with an
22 average speed of 0.6 cm s^{-1} . Below about 1500 m, along-isopycnal diffusiv-
23 ity is estimated to be $\sim 200\text{-}400 \text{ m}^2 \text{ s}^{-1}$.

24 **1. Introduction**

25 Water properties in the Canada Basin, in the Arctic Ocean, are set by the temperature and salin-
26 ity of the source waters and by the processes driving water mass evolution. In the deep Canada
27 Basin, the circulation and mixing environment are poorly understood, with limited direct observa-
28 tions of dissipation and velocity. In this paper, we focus on the deep water masses, found below
29 roughly 700 m depth. Using yearly hydrographic profile data from 2003 to 2015, we investigate
30 and quantify the processes driving changes in water mass properties using empirical orthogonal
31 function (EOF) analysis and an inverse method based on the tracer conservation equations adapted
32 for the deep Canada Basin.

33 Water masses in the Canada Basin are largely defined based on the origin of the inflow. Between
34 roughly 200 m and 2000 m depth, water of Atlantic origin enters the basin in a boundary current
35 and a series of intrusive features. The Atlantic Water is divided into two branches: Fram Strait
36 Branch Water (FSBW) and the deeper, cooler Barents Sea Branch Water (BSBW). BSBW is mod-
37 ified at the surface in the Barents Sea (Rudels et al. 2004) and found from roughly 700-2000 m
38 depth in the Canada Basin.

39 The dominant circulation features affecting the Atlantic Water are thought to be a narrow, topo-
40 graphically steered boundary current and the wind-driven Beaufort Gyre. The boundary current
41 transports Atlantic Water cyclonically around the basin, with inflow near the Northwind Ridge
42 and Chukchi Borderland (e.g., see Woodgate et al. 2007). Spall (2013) used an idealized eddy-
43 resolving numerical model to show that lateral eddy fluxes and vertical mixing in the basin interior
44 are likely important factors in driving the cyclonic Atlantic Water boundary current circulation.

45 The anticyclonic Beaufort Gyre characterizes the central basin circulation (Newton and Coach-
46 man 1974; McLaughlin et al. 2009; Proshutinsky et al. 2009; McPhee 2013). Analyzing data

47 between 1993 and 2007, McLaughlin et al. (2009) tracked a warm temperature anomaly in the
48 FSBW as it spread across the Canada Basin, and concluded that transport occurred through a com-
49 bination of advection by the gyre and lateral spreading in intrusions (i.e., thermohaline features
50 which were studied in detail by Walsh and Carmack (2002, 2003)). Woodgate et al. (2007) used
51 hydrographic data from a single expedition in 2002 to map anomalously warm FSBW and cool
52 BSBW intrusions from the boundary current across the Chukchi Borderland to the Canada Basin.

53 Below the BSBW lies a layer of relatively cool water, which forms a deep temperature minimum
54 in the Canada Basin centered around roughly 2500 m depth (Timmermans et al. 2003, 2005; Car-
55 mack et al. 2012). The \sim 500-1000 m thick Deep Temperature Minimum Layer (DTML) overlies
56 the Canada Basin bottom water. The relatively cool water in the DTML likely enters the Canadian
57 Basin from the Eurasian Basin (e.g., see Rudels et al. 2000), with the Canada Basin bottom wa-
58 ters likely being relic waters from previous dense water renewal hundreds of years ago (e.g., see
59 Macdonald et al. 1993; Timmermans and Garrett 2006).

60 The bottom water layer is vertically homogeneous in both temperature and salinity and is kept
61 well mixed by thermal convection driven by geothermal heat (Timmermans et al. 2003; Carmack
62 et al. 2012). Analyzing hydrographic data from 1993, 1997, and yearly from 2002 to 2010, Car-
63 mack et al. (2012) observed the DTML and homogeneous bottom water warming at a constant rate
64 of roughly 0.004°C per decade, which appears to be associated with a buildup of geothermal heat.
65 The presence of a deep double-diffusive staircase at the base of the DTML suggests limited turbu-
66 lent mixing of heat from the bottom water into the DTML, although there is evidence of enhanced
67 turbulent mixing and density overturns on the slope (Timmermans et al. 2003).

68 Velocity measurements are rare in these deep waters, and the weak flow magnitudes are difficult
69 to resolve. However, characterization of the flow field is possible through analysis of the temper-
70 ature and salinity fields. The goal of the present analysis is to investigate changes in water mass

71 properties and quantify lateral transport mechanisms in the deep Canada Basin from hydrographic
72 data. We begin by using EOF analysis to determine spatial and temporal variations in the proper-
73 ties of the BSBW and DTML water masses, and examine how properties vary with depth across
74 the basin. We infer dominant mechanisms of lateral transport of water mass properties, which are
75 further quantified by an inverse method.

76 The inverse method approach used is designed to determine the horizontal velocity field and
77 along-isopycnal diffusivity that best explain observed changes in tracers - here, temperature and
78 salinity - on isopycnal surfaces. Estimates are calculated from the best fit solution to an over-
79 determined set of equations derived from the temperature and salinity conservation equations
80 in advective-diffusive form. The velocity field is additionally constrained using a geostrophic
81 streamfunction, however the method does not require an assumed level of no-motion (or level of
82 known-motion); the magnitude of the advective velocity is determined based on the temperature
83 and salinity fields.

84 The inverse method is conceptually similar to those of Lee and Veronis (1991) and Zika et al.
85 (2010), although the results of the inversion are limited to along-isopycnal diffusivity and velocity,
86 rather than three-dimensional fields. Unlike the beta-spiral method (Stommel and Schott 1977)
87 or the Bernoulli inverse method (Killworth 1986), the method is based on changes in a tracer
88 field. To deal with the limitations inherent in the available data, and the small signals common to
89 the quiescent deep Arctic, the method used is deliberately simplistic. It is designed to provide an
90 order-of-magnitude estimate of the quantities of interest, which are then interpreted in combination
91 with the results of the EOF analysis.

92 In section 2, we describe the repeat hydrographic survey data used in the analysis and the typical
93 salinity and temperature structure observed in the deep Canada Basin. In section 3, we describe
94 the inverse method and discuss the requirements for its implementation. Section 4 presents results

95 from the EOF analysis that qualitatively and quantitatively describe water mass changes. Section 5
96 presents results from the inverse method and estimates of lateral advective velocity and diffusivity
97 for each water mass. These results, in combination with the results of the EOF analysis, are
98 discussed and summarized in section 6.

99 **2. Data and Water Mass Description**

100 *a. Repeat hydrographic profiles*

101 Full-depth repeat hydrographic profiles were collected yearly in the Canada Basin during
102 summer surveys of the Joint Ocean and Ice Studies (JOIS) and Beaufort Gyre Observing
103 System (BGOS) programs; we use data from 2003 to 2015 which are available online at
104 www.whoi.edu/beaufortgyre. Conductivity-Temperature-Depth (CTD) instrument resolution is
105 ~ 0.0002 for salinity and 0.0003°C for temperature. CTD instrument accuracy is ± 0.002 for salin-
106 ity, $\pm 0.001^{\circ}\text{C}$ for temperature, and ± 2 m for depth (see Carmack et al. 2012). We use 1 m
107 vertically averaged data.

108 The typical hydrographic sampling pattern (Figure 1a) provides approximately repeat spatial
109 coverage. The Canada Basin is 3500-3800 m deep, with a slope in the southeast. A limited
110 number of hydrographic profiles are available from the basin margins and the slope. The analysis
111 is restricted to profiles in the deep Canada Basin, which we define as locations where the ocean
112 bottom depth exceeds 3000 m, determined using the International Bathymetric Chart of the Arctic
113 Ocean (IBCAO) (Jakobsson et al. 2012). The influence of processes on the slope and near the
114 basin margins is discussed in section 6.

115 *b. Water mass properties*

116 Typical temperature and salinity profiles are shown in Figure 1b,c. Below a shallow mixed
117 layer and water of Pacific origin, two branches of the Atlantic Water enter the basin in a series of
118 thermohaline intrusions, which are visible in a temperature-salinity (T - S) diagram as ‘zig-zags’
119 (Figure 1b). Temperature and salinity increase with depth to the FSBW temperature maximum.
120 Below the FSBW, smaller but more numerous intrusions carry cool BSBW from the boundary cur-
121 rent into the deep basin. The thermohaline intrusions observed in the FSBW and BSBW spread
122 laterally on near-isopycnal surfaces across Arctic basins (Carmack et al. 1998), exchanging prop-
123 erties through double-diffusive fluxes. The intrusions gradually change density as they spread as
124 a result of vertical flux divergences, which are hypothesized to drive lateral fluxes (Carmack et al.
125 1998). Intrusions were first observed in the Canadian Basin in 1993 (Carmack et al. 1995), and
126 had spread across the central Canada Basin by 2003 (McLaughlin et al. 2009). The DTML is char-
127 acterized by a minimum in potential temperature at roughly 2500 m depth, below which presumed
128 double-diffusive layers are evident (Timmermans et al. 2003, Figure 1c (inset)).

129 The analysis here focuses on the BSBW and DTML, but also includes the FSBW, to enable
130 comparison with a water mass for which the dynamics are better understood. Since the bottom
131 water below the DTML is vertically and approximately laterally homogeneous (Carmack et al.
132 2012), it is not included in the analysis. We consider temperature and salinity variations along
133 isopycnals (defined using potential density referenced to the surface). As discussed in Zika et al.
134 (2010), determining the magnitude of advection and diffusion of tracers using an inverse method
135 is best accomplished in an isopycnal reference frame. The use of potential density referenced
136 to the surface as opposed to a deeper level does not significantly impact the results, either qual-
137 itatively or quantitatively. In particular, if a deep reference level (e.g., 1000 m) is used instead,

138 the resulting estimates of diffusivity and velocity are well within the estimated uncertainty. The
139 28.097 kg m^{-3} isopycnal (potential density anomaly) is referred to as characteristic of the DTML,
140 and the 28.010 kg m^{-3} and 27.925 kg m^{-3} isopycnals as characteristic of the BSBW and the
141 FSBW, respectively.

142 We focus on potential temperature as the tracer of interest, and note that temperature and salinity
143 are interdependent but effectively passive tracers on isopycnals in the deep Canada Basin. A given
144 temperature anomaly is density-compensated by changes in salinity on an isopycnal, with salinity
145 variations an order of magnitude smaller than temperature variations. Results are reported only
146 for the potential temperature field, however we find that they are qualitatively and quantitatively
147 similar (to well within uncertainty) if salinity is used instead.

148 *c. Time evolution*

149 Observations indicate that the temperature of each of the three water masses of interest varies
150 over the course of the record (Figure 2). The FSBW in the central Canada Basin exhibits a general
151 warming since 2003, the BSBW cooled at a constant rate over the course of the record from 2003
152 to 2015, while the DTML gradually warmed over the same time period.

153 The FSBW entering the Canada Basin in the early 2000s was characterized by anomalously
154 warm maximum temperatures, $> 0.5^\circ\text{C}$ up to $\sim 1^\circ\text{C}$, and increased salinity (McLaughlin et al.
155 2009). The warming trend in the FSBW in the Canada Basin began to level off in the mid-2000s,
156 reflecting changes in the temperature of the boundary current inflow.

157 Between 2003 and 2015, the BSBW on $\sigma = 28.01 \text{ kg m}^{-3}$ cooled by $-2.8 \times 10^{-3} \text{ }^\circ\text{C yr}^{-1}$ and
158 freshened at a rate of $-1.9 \times 10^{-4} \text{ yr}^{-1}$, with similar rates of cooling and freshening at all stations
159 within the deep basin. This change in water properties occurred at an approximately constant rate
160 over the time period of interest. Woodgate et al. (2007) observed a cold anomaly in the BSBW in

161 the Chukchi Borderland in 2002 with temperatures up to 0.5°C colder than the mean, associated
162 with continual cooling and freshening of the inflow in the boundary current.

163 Between 2003 and 2015, the DTML on $\sigma = 28.097 \text{ kg m}^{-3}$ warmed at a nearly constant rate
164 of $3.5 \times 10^{-4} \text{ }^{\circ}\text{C yr}^{-1}$, with a linear increase in salinity of $2.2 \times 10^{-5} \text{ yr}^{-1}$; these trends are of the
165 opposite sign and an order of magnitude smaller than the temperature and salinity trends character-
166 izing the BSBW. Carmack et al. (2012) related warming of the DTML to geothermal heating; we
167 additionally seek to address spatial variations in the temperature of the DTML, including lateral
168 gradients and the presence of anomalously warm water near the basin margins and on the slope.

169 *d. Spatial variations*

170 Spatial patterns associated with the temperature of each water mass are presented qualitatively
171 by objectively mapping all hydrographic profile data from 2003 to 2015, after first subtracting the
172 isopycnal-mean potential temperature anomaly for each year (Figure 3). Temperature variations
173 are qualitatively different for each water mass, reflecting the inflow of cold BSBW in the boundary
174 current, as opposed to warm anomalies for the FSBW and DTML.

175 The warmest FSBW is near the boundary current inflow at the northern part of the Northwind
176 Ridge. McLaughlin et al. (2009) related warming of the FSBW in the north of the Canada Basin
177 to northeastward advection by the anticyclonic Beaufort Gyre. The BSBW is coldest near the
178 boundary current inflow, with a clear east-west temperature gradient ($\mathcal{O}(10^{-7} \text{ }^{\circ}\text{C m}^{-1})$ on $\sigma =$
179 28.01 kg m^{-3}). The DTML has a similar spatial pattern to that of the BSBW in the deep basin,
180 but with the opposite sign gradient; warmer in the west and cooler in the east ($\mathcal{O}(10^{-8} \text{ }^{\circ}\text{C m}^{-1})$
181 on $\sigma = 28.097 \text{ kg m}^{-3}$). The warmest water in the DTML is on the slope in the southeast and
182 near the basin margins, rather than in the northern basin as for the FSBW. These spatial patterns
183 are similar on all isopycnals within each water mass, and are quantified in section 4.

184 **3. Inverse Method Theory**

185 The inverse method originates from the tracer conservation equation in advective-diffusive form.
186 Our goal is to determine large-scale lateral velocity and diffusivity estimates that best explain the
187 observed tracer distribution. We make several simplifying assumptions, the validity of which are
188 discussed further in the following sections.

189 We assume that across-isopycnal transport has a negligible effect on tracer properties relative to
190 along-isopycnal transport. The presence and persistence of intrusions (Walsh and Carmack 2002,
191 2003) and double-diffusive staircases (Timmermans et al. 2003, 2008; Bebieva and Timmermans
192 2016) in the Canada Basin reflect low levels of mechanical mixing supported by observations
193 (Rainville and Winsor 2008; Guthrie et al. 2013; Dosser and Rainville 2016). This assumption is
194 likely inappropriate on the slope and near the margins of the basin, where the absence of a deep
195 double-diffusive staircase suggests enhanced turbulent mixing (Timmermans et al. 2003).

196 Along-isopycnal eddy processes are parameterized in terms of a lateral diffusivity, κ_H , following
197 the standard Reynolds averaging approach, and this lateral diffusivity is assumed to be approxi-
198 mately constant on any isopycnal. This is likely a poor approximation, as it is known that eddy
199 kinetic energy varies across the Canada Basin (Zhao et al. 2016), and as such the diffusivity should
200 be treated as an approximate average on a given isopycnal.

201 There is no significant trend in the spacing between isopycnals in the deep water masses. Further,
202 hydrographic profiles represent only a single snapshot of the basin stratification for each year.
203 Therefore, divergence and convergence between isopycnals is not explicitly accounted for in the
204 governing equations. The effect of eddy fluxes on along-isopycnal transport of tracer is captured
205 by the lateral diffusion term.

206 Applying the above assumptions to the advective-diffusive form of the potential temperature (θ)
 207 conservation equation, and assuming no sources or sinks in the deep basin, yields:

$$\frac{\partial \theta}{\partial t} + u_g \frac{\partial \theta}{\partial x_\sigma} + v_g \frac{\partial \theta}{\partial y_\sigma} = \kappa_H \left(\frac{\partial^2 \theta}{\partial x_\sigma^2} + \frac{\partial^2 \theta}{\partial y_\sigma^2} \right),$$

208 where x_σ and y_σ are defined as the lateral, along-isopycnal coordinates, with z_σ as the normal,
 209 across-isopycnal coordinate. Hereafter we drop the ‘ σ ’ on x, y, z and use subscripts for deriva-
 210 tives. Assuming that lateral circulation is predominantly geostrophic, the geostrophic velocity
 211 $\vec{u}_g = (u_g, v_g)$ may be written in terms of a streamfunction ψ as $u_g = -\partial_y \psi$, $v_g = \partial_x \psi$. Here these
 212 velocities represent flow along isopycnal surfaces:

$$\partial_t \theta - \partial_y \psi \partial_x \theta + \partial_x \psi \partial_y \theta = \kappa_H (\partial_{xx} \theta + \partial_{yy} \theta). \quad (1)$$

213 The direction and magnitude of the velocity field are determined separately, which begins by
 214 writing the streamfunction in separable form: $\psi(x, y, z) = \Psi(z) \tilde{\psi}(x, y)$. Here Ψ is a streamfunction
 215 amplitude determined from the inverse method (section 5a), and $\tilde{\psi}$ captures the spatially varying
 216 component of the streamfunction (i.e., defines the shape of streamfunction contours, section 4e).

217 Vertical velocity is assumed to be negligible for the gyre flow over the deep Canada Basin
 218 abyssal plain (where variations in the Coriolis parameter are negligible, i.e., an f-plane); as a
 219 consequence, on a given horizontal surface, horizontal pressure gradients are everywhere paral-
 220 lel to horizontal density gradients (see e.g., Hughes and Killworth 1995). Contours of constant
 221 density on a horizontal plane therefore have the same shape as geostrophic streamfunction con-
 222 tours, $\tilde{\psi}$. Note that to estimate $\tilde{\psi}$ in isopycnal coordinates (section 4e), depth contours of a given
 223 isopycnal are used (equivalent to the use of isopycnal contours at a given depth level). Then
 224 $\vec{u}_g = \Psi(-\partial_y \tilde{\psi}, \partial_x \tilde{\psi}) = \Psi(\tilde{u}_g, \tilde{v}_g)$, and (1) becomes:

$$\partial_t \theta + \Psi (\tilde{u}_g \partial_x \theta + \tilde{v}_g \partial_y \theta) = \kappa_H (\partial_{xx} \theta + \partial_{yy} \theta). \quad (2)$$

225 The streamfunction is normalized so that $|(\tilde{u}_g, \tilde{v}_g)|$ has unit mean. In this way, Ψ determines the
 226 magnitude of the velocity field, while $(\tilde{u}_g, \tilde{v}_g)$ set the direction of flow at each spatial location. We
 227 rearrange (2) as follows:

$$\frac{(\tilde{u}_g \partial_x \theta + \tilde{v}_g \partial_y \theta)}{\partial_t \theta} = \frac{\kappa_H}{\Psi} \frac{(\partial_{xx} \theta + \partial_{yy} \theta)}{\partial_t \theta} - \frac{1}{\Psi} \quad (3)$$

228 such that κ_H/Ψ represents the slope of a line with intercept $-1/\Psi$. An analogous equation holds
 229 for salinity.

230 Equation (3) may be formulated to be independent of time, an approximation based on the
 231 observation that $\partial_t \theta$ and $\partial_t S$ are approximately constant over the course of the record, in both the
 232 BSBW and DTML (section 2c). Further, similar values of $\partial_t \theta$ and $\partial_t S$ are found at all stations
 233 within the deep basin (ocean bottom depth > 3000 m), which implies that spatial gradients do not
 234 change significantly between years. The accuracy of this approximation is examined in detail as
 235 part of the EOF analysis (section 4c). Equation (3) may then be expressed as:

$$\tau_1(x, y) = \frac{\kappa_H}{\Psi} \tau_2(x, y) - \frac{1}{\Psi}, \quad (4)$$

236 where $\tau_1(x, y)$, estimated from observations, is an advective fraction representing changes in the
 237 temperature field associated with along-isopycnal advection, while $\tau_2(x, y)$ is a diffusive fraction
 238 representing variations associated with parameterized along-isopycnal diffusivity. Equation (4)
 239 has two unknowns, Ψ and κ_H , and is valid on any isopycnal in the BSBW or DTML water masses.
 240 A least-squares linear fit to (4) yields Ψ and κ_H .

241 The streamfunction amplitude Ψ has units of diffusivity ($\text{m}^2 \text{s}^{-1}$), so that the dimensionless ratio
 242 κ_H/Ψ in (4) can be treated as a measure of the relative importance of along-isopycnal diffusion
 243 to advection in the evolution of the temperature (or salinity) field. For a ‘diffusive-advective ratio’
 244 greater than unity, lateral diffusion is the dominant driver of changes in water mass temperature

245 and salinity, whereas advection dominates for $\kappa_H/\Psi < 1$. It is of interest to note that this ratio
246 could be interpreted as an inverse Peclet number.

247 The calculation of spatial derivatives in (4) is non-trivial. Sparse data in some regions and scatter
248 in the potential temperature field result in large uncertainties and discrepancies when calculating
249 derivatives, and (4) requires second-order derivatives. Interpolating θ and S on an isopycnal using
250 techniques such as objective mapping (Figure 3) create smoothly varying fields but are highly
251 sensitive to outlying measurements, which may or may not be physical, increasing the uncertainty
252 when taking derivatives. To more carefully quantify variations in properties in the deep water
253 masses, we turn to EOF analysis.

254 **4. Empirical Orthogonal Function Analysis**

255 Our goal in using EOF analysis is twofold: to quantify changes in water mass properties in the
256 deep Canada Basin, and to isolate the dominant spatial patterns in the potential temperature field
257 in order to calculate large-scale, low-noise spatial derivatives for use with the inverse method.

258 *a. Implementation*

259 EOF analysis produces a set of ordered orthogonal modes - that is, the minimum number of
260 independent patterns needed to capture the maximum amount of variance in the data. Spatial EOF
261 modes are extracted for data sampled at different isopycnal levels (Appendix), so that the principal
262 components (PCs) show how the spatial modes vary between isopycnals (see e.g., Gavart and De
263 Mey 1997). Measurements of the form $A(\vec{x}, z)$ are used, where A is a water property such as
264 potential temperature or salinity. A separate EOF analysis is performed for each year, then the
265 dominant modes for all years are compared.

266 The method is described by way of example (Figure 4) with reference to potential temperature
267 on isopycnals for a specific year (2004). Analysis is restricted to profiles in the deep basin, defined
268 as locations with ocean bottom depths >3000 m. Isopycnals are chosen such that the average
269 isopycnal depths are equally spaced between 300 and 3000 m, for 50 isopycnals from $\sigma = 27.8$
270 to 28.1 kg m^{-3} . EOF analysis identifies spatial patterns in temperature common to the FSBW,
271 BSBW, and DTML water masses. Before the EOF analysis is performed, the potential temperature
272 field on each isopycnal is normalized to have zero mean and unit standard deviation, which ensures
273 the results are not biased towards isopycnals with larger amplitude temperature variations.

274 The first and second EOF modes for 2004, and the associated PCs, are shown in Figure 4a,c.
275 The sign of each mode on a given isopycnal is determined from the sign of the associated PC. The
276 first EOF mode captures predominantly longitudinal variations in potential temperature (Figure
277 4a), and captures 56% of the total variance in the normalized data (Appendix, Figure 4b), while
278 the second mode has predominantly latitudinal variations, and captures 25% of the total variance.
279 The first and second modes together capture 81% of the variance in the normalized data. There is
280 a clear separation between the variance explained by the first two modes and that explained by the
281 third and higher modes (Figure 4b). Modes higher than 5 are indistinguishable from noise.

282 The PCs provide the amplitude of each EOF mode on each isopycnal (Figure 4c). The BSBW
283 temperature field (~ 700 - 1500 m), for example, is well described by the first EOF mode alone (Fig-
284 ure 4a, with opposite sign), consistent with qualitative observations of an east-west temperature
285 gradient (Figure 3b). The first EOF mode is also dominant within the DTML, while the first and
286 second modes are important in the FSBW and near the base of the DTML in the double-diffusive
287 staircase (Figure 4c).

288 *b. Interpretation of spatial modes*

289 The spatial modes arising from the EOF analysis are statistical constructs assigned meaning
290 based on existing knowledge of the system. While a single mode will never perfectly capture
291 an underlying physical principle, they can provide insight into the physics governing a system.
292 The first EOF mode (Figure 4a) shows primarily a longitudinal gradient in temperature, consistent
293 with warm (FSBW, DTML) or cold (BSBW) temperature anomalies diffusing along isopycnals,
294 from the boundary current in the west into the deep basin. The fact that the first EOF mode is
295 the dominant mode in the two deep water masses suggests that along-isopycnal diffusion may be
296 the dominant process controlling changes in water mass properties, a hypothesis which will be
297 explored further using the inverse method in section 5.

298 The second EOF mode shows a predominantly latitudinal temperature gradient, and is of oppo-
299 site sign in the FSBW (warmer to the north) and the DTML (warmer to the south). In the FSBW,
300 the second mode is likely associated with the anticyclonic Beaufort Gyre circulation. McLaugh-
301 lin et al. (2009) linked advection by the gyre to warm temperature anomalies travelling from the
302 boundary current across the northern basin. This interpretation is consistent with the stronger in-
303 fluence of the second mode on the FSBW relative to the BSBW (Figure 4c), as the gyre is assumed
304 to decrease in strength with depth. In the DTML, the second EOF mode is associated with anoma-
305 lously warm temperatures in the southern basin, with possible sources near the margins and on the
306 slope to the south. This is inconsistent with advection by an anticyclonic gyre, but may be linked
307 to enhanced mechanical mixing or cyclonic advection, to be discussed further in sections 5 and 6.

308 *c. Similarity of EOF modes through time*

309 A separate EOF analysis is conducted for each year, and the resulting modes are compared. The
310 EOF modes and PCs for a given year are calculated using potential temperature profiles from only

311 that year. The isopycnals used are the same for all years, as is the restriction to profiles in the deep
312 basin (bottom depth >3000 m). If the processes driving changes in water mass properties in the
313 deep basin do not change significantly between years, we would expect similar EOF modes for all
314 years.

315 From 2003 to 2015, the first EOF mode corresponding to each year explains between 45 and
316 70% of the total variance in the normalized potential temperature data for the FSBW, BSBW, and
317 DTML water masses in the deep Canada Basin. The second mode explains 15 to 35%, for a
318 combined total of 70 to 85% variance explained by two modes alone. We conclude that the first
319 two modes are sufficient to describe the water masses of interest for all years.

320 Spatial correlations quantify the similarity between the EOF modes from different years. To
321 perform a correlation, the EOF mode is first mapped onto a 1° latitude by 4° longitude grid (Figure
322 5b). If more than one data point falls within a grid box, the average value is used. To calculate the
323 correlation coefficient, r , between any two years, only grid boxes with data available for both years
324 are included. Due to the approximately repeat sampling pattern for the hydrographic stations, all
325 years have most grid boxes in common.

326 The spatial patterns for the first EOF mode have high correlations between years, for all years
327 from 2003 to 2015 (Figure 5a), with $r \geq 0.75$. Therefore, the dominant feature of the potential
328 temperature field in the deep Canada Basin over the last decade has been a persistent east-west
329 gradient, despite temporal changes in the average temperature of each water mass. Correlation co-
330 efficients for the second EOF mode for all years range from $r = 0.55$ to $r = 0.95$ (not shown), sug-
331 gesting that the dominant processes controlling variations in water mass properties do not change
332 significantly during the 13 years considered.

333 *d. Structure in the vertical*

334 The principal components provide the amplitude of each EOF mode on each isopycnal. The
335 mode amplitude is converted into percent variance explained by the first and second mode on
336 each isopycnal for each year (Appendix, Figure 6). (This is equivalent to calculating variance
337 by correlating the temperature field reconstructed from EOF mode 1 or 2 (Appendix) with the
338 observed potential temperature field.) For example, the PC associated with the first EOF mode
339 in 2004 has an amplitude close to 1 in the BSBW (Figure 4c) and explains nearly 100% of the
340 variance in the BSBW potential temperature data (Figure 6a, second column). The total variance
341 explained by the first (or second) EOF mode is the average over all isopycnals for each year.

342 Potential temperature on isopycnals in the FSBW is described primarily by the second EOF
343 mode (Figure 6b), for all years except 2003 and 2004 when the first mode contributes significantly.
344 After about 2004, the FSBW flowing into the Canada Basin no longer displayed the warming trend
345 observed by McLaughlin et al. (2009) (Figure 2), which may account for the shift. The sign of the
346 second mode is the same for all years (not shown), with warmer waters to the north.

347 For both the BSBW and DTML, the first EOF mode explains the majority of the temperature
348 variance (usually 75% or higher) on most isopycnals, for all years (Figure 6a), with spatial vari-
349 ations dominated by a basin scale east-west gradient. The second EOF mode is intermittently
350 important for a narrow range of isopycnals between the two water masses (centered slightly above
351 2000 m depth), where the sign of the temperature gradient reverses (cool vs. warm anomaly), as
352 well as in the deep double-diffusive staircase, where warmer waters are consistently found to the
353 south of the basin. For isopycnals between the BSBW and DTML, variations in temperature are
354 significantly smaller than for either water mass, and the second EOF mode likely has no consistent
355 physical interpretation. Its interpretation in the deep staircase is discussed in section 6.

356 Both the first and second EOF modes are highly persistent between 2003 and 2015, with similar
357 contributions to the temperature field on isopycnals throughout both the BSBW and DTML water
358 masses. This indicates that along-isopycnal temperature gradients are qualitatively and quantita-
359 tively similar between years, which is consistent with the initial observation that the constant rate
360 of cooling (BSBW) and warming (DTML) showed minimal variation between stations (Figure 2,
361 section 2c). The temporal coherence of the EOF modes and associated PCs further suggests that
362 the physical processes driving changes in water mass properties do not change between 2003 and
363 2015.

364 *e. Isopycnal depth and the streamfunction*

365 A similar EOF analysis to that for temperature is conducted for isopycnal depth to determine the
366 geostrophic streamfunction contours, as defined in section 3. The magnitude of the geostrophic
367 velocity field is determined from the inverse method, while the streamfunction contours on each
368 isopycnal, $\tilde{\psi}(x,y)$, are determined using depth contours of a given isopycnal.

369 An EOF analysis of the isopycnal depth field is performed for each year from 2003 to 2015. The
370 first EOF mode (Figure 7b) captures the majority of the variability in isopycnal depth for all years,
371 explaining between 75-90% of the variance, with an average of 84%. The PC associated with the
372 first EOF mode does not change sign with depth - that is, all isopycnals deepen toward the center
373 of the Beaufort Gyre, forming a bowl-shape centered near 74°N and 153°W . Unlike the EOFs for
374 potential temperature, the second EOF mode for isopycnal depth explains less than 10% of the
375 total variance on average, and likely does not have a consistent physical interpretation.

376 Correlations between the first EOF mode for isopycnal depth for each year with every other year
377 show reasonable similarity between years (Figure 7a), with correlation coefficients of between 0.5
378 and 1.0. In 2012, isopycnals were flatter than during other years, perhaps reflecting observations

379 that show an expansion of the Beaufort Gyre since 2007 (McPhee 2013). The mode 1 spatial
380 patterns from 2003 to 2015 are appropriately normalized and grid-averaged to produce a time-
381 independent $\tilde{\psi}$ (Figure 7b, section 3, section 5a).

382 **5. Inverse Method Results**

383 The goal of the inverse method analysis is to estimate geostrophic velocity and along-isopycnal
384 diffusivity on isopycnals within the BSBW and DTML water masses, and relate these to circulation
385 and transport of water mass properties.

386 *a. Inverse method implementation*

387 Spatial derivatives in (4) are calculated using a 2-mode reconstruction of the potential temper-
388 ature field from the EOF analysis (Appendix, Figure 8), reintroducing dimensional units. When
389 calculating the 2-mode reconstruction, the standard deviation of temperature on each isopycnal is
390 reintroduced, but the mean is not, which effectively removes the temporal trend from the data.

391 The reconstructed fields are translated onto a 1° latitude by 4° longitude grid, as shown for $\tilde{\psi}$
392 in Figure 7b. The size of a grid box is chosen to be consistent with the station spacing, with an
393 associated length scale on the order of 100 km. Of course, the parameterized diffusivity κ_H is
394 sensitive to the station spacing and length scale. The value of temperature within a grid box is the
395 average of all data points within the grid box from all years. Since spatial gradients in temperature
396 on an isopycnal vary negligibly in time between 2003 and 2015 (section 4), it is appropriate to
397 combine data from all years to calculate derivatives (using centered finite differences), reducing
398 uncertainty. Gridding the data and taking discrete derivatives imposes a length-scale on the results,
399 but permits the calculation of first- and second-order spatial derivatives that reflect the observed
400 large-scale, slowly-varying gradients in tracer fields.

401 Equation (4) is evaluated in each grid box on a given isopycnal, then a least-squares linear fit to
 402 τ_1 and τ_2 is used to determine the slope and intercept, from which Ψ , κ_H , and their uncertainties
 403 are calculated. The full geostrophic velocity field is then reconstructed from $u_g = -\Psi \partial_y \tilde{\psi}$, $v_g =$
 404 $\Psi \partial_x \tilde{\psi}$. Grid boxes are excluded when discrete spatial derivatives cannot be properly calculated
 405 due to lack of data in adjacent grid boxes.

406 *b. Inverse method results for the BSBW*

407 We report results for isopycnals from $\sigma = 27.98 \text{ kg m}^{-3}$ (with an average depth of $\sim 700 \text{ m}$)
 408 to $\sigma = 28.06 \text{ kg m}^{-3}$ (average depth $\sim 1500 \text{ m}$) in the BSBW, and use $\sigma = 28.01 \text{ kg m}^{-3}$ as a
 409 representative example (Figure 9). The inverse method least-squares linear fit (Figure 9a) has $r^2 =$
 410 0.5. Out of 52 grid boxes containing data, 3 were discarded from the final fit due to the inability
 411 to calculate discrete derivatives. The slope gives a diffusive-advective ratio of $\kappa_H/\Psi = 2.0 \pm 0.3$.
 412 The intercept gives a streamfunction amplitude of $\Psi = 214 \pm 32 \text{ m}^2 \text{ s}^{-1}$. Lateral diffusivity along
 413 the $\sigma = 28.01 \text{ kg m}^{-3}$ isopycnal is then estimated to be $\kappa_H = 400 \pm 88 \text{ m}^2 \text{ s}^{-1}$.

414 The average magnitude of the advective velocity field along $\sigma = 28.01 \text{ kg m}^{-3}$ is $|\vec{u}_g| = 0.33 \pm$
 415 0.08 cm s^{-1} . Flow speeds in individual grid boxes range from $|\vec{u}_g| = 0.05$ to 0.5 cm s^{-1} . The
 416 full geostrophic velocity field on this isopycnal (Figure 9b) is anticyclonic, with the isopycnal
 417 deepening to $\sim 1000 \text{ m}$ depth at the gyre center. Water appears to enter the basin moving eastward
 418 from the northern end of the Northwind Ridge.

419 Values for κ_H/Ψ for isopycnals within the BSBW range from 1.5 to 2.0, with an average value
 420 of 1.6 above about 1200 m, after which values decline with depth. Average velocity magnitudes
 421 on individual isopycnals within the BSBW range from $|\vec{u}_g| = 0.3$ to 1.2 cm s^{-1} , with an overall
 422 average for the BSBW of 0.6 cm s^{-1} . There is no significant trend in velocity magnitude with

423 depth. Lateral diffusivity on isopycnals within the BSBW ranges from $\kappa_H = 205$ to $833 \text{ m}^2 \text{ s}^{-1}$,
424 with an average value of $462 \text{ m}^2 \text{ s}^{-1}$.

425 The estimated values of the diffusive-advective ratio suggest that lateral diffusivity plays a dom-
426 inant role in tracer transport in the BSBW above ~ 1200 m depth, being nearly twice as important
427 to along-isopycnal variations in temperature and salinity as the geostrophic gyre circulation. This
428 result is consistent with the EOF analysis results, where the first EOF mode - with primarily lon-
429 gitudinal variations consistent with eastward diffusion of anomalies transported by the boundary
430 current along the western basin margin - explains most of the variance in the BSBW tempera-
431 ture and salinity fields (Figure 6a). The second EOF mode, which is more likely associated with
432 transport by the anticyclonic gyre, plays a secondary role in the BSBW (Figure 9b).

433 In the deepest part of the BSBW (from $\sim 1500 - 2000$ m), the inverse method predicts cyclonic
434 gyre circulation. This would suggest that the lateral pressure gradient at these depths has the
435 opposite sign from that at shallower depths, such that the gradient is from low (in the gyre center)
436 to high (at the periphery). This reversal of the gyre would also require that the geostrophic velocity
437 pass through zero at some depth in the deep BSBW; inverse method results close to the transition
438 are inherently uncertain, and are not reported here.

439 *c. Results for the DTML*

440 In the DTML, the inverse method predicts cyclonic gyre circulation, so that Ψ is negative.
441 We include isopycnals from $\sigma = 28.090 \text{ kg m}^{-3}$ (with an average depth of ~ 2000 m) to
442 $\sigma = 28.102 \text{ kg m}^{-3}$ (average depth ~ 2800 m) in the DTML. Values for κ_H/Ψ are close to zero
443 at the top and bottom of the DTML and within the double-diffusive staircase, and range from -1.3
444 to -1.8 within the core of the water mass, with an average of -1.6. Average velocity magnitudes
445 on isopycnals within the core of the DTML range from $|\vec{u}_g| = 0.2$ to 0.4 cm s^{-1} , with an overall

446 average of 0.3 cm s^{-1} . Lateral diffusivity ranges from $\kappa_H = 198$ to $393 \text{ m}^2 \text{ s}^{-1}$, with an average
447 value of $305 \text{ m}^2 \text{ s}^{-1}$, then declines rapidly in the staircase. On $\sigma = 28.097 \text{ kg m}^{-3}$, values are
448 $\kappa_H/\Psi = -1.8 \pm 0.5$, $\kappa = 292 \pm 127 \text{ m}^2 \text{ s}^{-1}$, and $|\vec{u}_g| = 0.2 \pm 0.1 \text{ cm s}^{-1}$.

449 The advective-diffusive ratio in the DTML suggests that along-isopycnal diffusivity is more
450 important than advection by the gyre to setting water mass properties. However, we note that it
451 is possible that the presence of a warm θ anomaly in the southern deep basin causes the inverse
452 method to incorrectly predict cyclonic gyre flow (in contrast to the FSBW which had a warm
453 anomaly in the north associated with anticyclonic transport by the gyre). Depending on the source
454 of this warm anomaly, the assumptions used in the inverse method may not apply in the DTML,
455 invalidating the results.

456 In particular, the assumption that vertical mixing is negligible may be inappropriate for the
457 DTML. Timmermans et al. (2003) found evidence of enhanced turbulent mixing in the DTML
458 on the slope in the southeast basin, and noted that the deep double-diffusive staircase was eroded
459 there. The staircase is also absent in the southwest in the deep basin (Figure 10). Vertical mixing
460 would warm the DTML, drawing (geothermal) heat and salt up from the homogeneous bottom
461 layer below (Carmack et al. 2012), with the largest fluxes in the boundary regions. Note also that
462 the highest temperatures are found along the presumed trajectory of the cyclonic boundary current
463 (Figure 10), suggesting advection by the boundary current may play a role.

464 Even if the prediction of cyclonic gyre flow is incorrect, results from the EOF analysis support
465 the conclusion that along-isopycnal diffusion is the dominant mechanism transporting heat from
466 the margins into the deep basin in the DTML. As in the BSBW, the first EOF mode explains the
467 majority of the variance in the DTML above the deep double-diffusive staircase (Figure 6). The
468 second EOF mode in the DTML may be related to cyclonic gyre flow, turbulent vertical mixing,
469 advection by the boundary current, or some combination thereof.

470 **6. Summary and Discussion**

471 Using a novel inverse method based on tracer conservation in combination with EOF analysis
472 of hydrographic data, we investigated the processes driving changes in water mass properties be-
473 tween 2003 and 2015 in the deep Canada Basin. Water mass transport was hypothesized to occur
474 through a combination of advection by the large-scale Beaufort Gyre circulation and lateral dif-
475 fusion of tracers from the basin margins. For both the BSBW and DTML deep water masses,
476 along-isopycnal diffusivity appears to be the dominant process controlling changes in temperature
477 and salinity in the deep basin, with relatively weak advection by the gyre. Both the gyre circula-
478 tion and along-isopycnal diffusivity seem to be important in the FSBW, with the influence of the
479 gyre dominating observed changes in tracer fields after 2004, as the rate of warming of the inflow
480 tapered off.

481 Cooling and freshening was observed in the BSBW, while the DTML became warmer and saltier.
482 In both deep water masses considered, EOF analysis was used to quantify changes in water mass
483 properties. Potential temperature for a given isopycnal in these water masses changed at a steady
484 rate through time from 2003 to 2015, with little variation between stations. Along-isopycnal tem-
485 perature and salinity gradients were approximately constant between years, and varied primarily
486 from east to west in both the BSBW and the DTML, consistent with lateral diffusion. Smaller
487 north-south gradients were linked to the Beaufort Gyre in the BSBW and to either the gyre or to
488 vertical (geothermal) heat fluxes near the basin margins in the DTML.

489 In the BSBW, an approximate geostrophic velocity field consistent with anticyclonic Beau-
490 fort Gyre circulation was determined by combining the results of the inverse method with a
491 geostrophic streamfunction with ~ 100 km horizontal resolution. The overall average speed of
492 along-isopycnal advection was $|\vec{u}_g| \sim 0.6 \text{ cm s}^{-1}$. In the DTML, cyclonic circulation was pre-

dicted, with $|\vec{u}_g| \sim 0.3 \text{ cm s}^{-1}$ on average. Beaufort Gyre current speeds below the FSBW in the central basin have previously been estimated to be 0-2 cm s^{-1} , with large uncertainty (Newton and Coachman 1974). The center of the gyre was located near 74°N and 153°W , in reasonable agreement with recent results from Armitage et al. (2017), who observed the center of the Beaufort Gyre shifting northwest between 2003 and 2014, from $\sim 74^\circ\text{N}$ and 145°W to $\sim 76^\circ\text{N}$ and 150°W .

From the inverse method, lateral diffusivity is estimated to be $\kappa_H \sim 450 \pm 150 \text{ m}^2 \text{ s}^{-1}$ in the BSBW and $\kappa_H \sim 300 \pm 100 \text{ m}^2 \text{ s}^{-1}$ in the DTML, with an associated length scale of 100 km corresponding to the average grid spacing. We note that values of diffusivity from the inverse method are sensitive to this grid spacing length scale, which is itself determined by the hydrographic station spacing. Here the lateral diffusivity accounts for any process that mixes potential temperature (or salinity) anomalies along isopycnals (contributions from e.g., eddy fluxes and thermohaline intrusions). The contribution of along-isopycnal diffusion to the evolution of tracer fields is estimated to be up to twice as important as advection by the Beaufort Gyre circulation.

More direct estimates of eddy diffusivity (i.e., based on velocity fluctuations) are rare in the Arctic Ocean. For the oceans south of 60°N , Cole et al. (2015) estimated along-isopycnal diffusivities at 300 km scale using Argo profile data. Below $\sim 1000 \text{ m}$ depth, they found zonally averaged values of order 100-1000 $\text{m}^2 \text{ s}^{-1}$. Employing a similar framework to Cole et al. (2015), Meneghello et al. (2017) estimate lateral diffusivities in the Canada Basin from velocity measurements to be $\sim 100 \text{ m}^2 \text{ s}^{-1}$ on average at depths around 600 m, with an associated length scale of around 50 km. Near the basin margins and the Chukchi Plateau, Meneghello et al. (2017) found diffusivities elevated by a factor of 3 or more, associated with a more active eddy field.

The estimate of lateral diffusivity found here for the BSBW is significantly higher than previous estimates associated with thermohaline intrusions alone. Walsh and Carmack (2002, 2003) analyzed thermohaline intrusions in the Canada Basin FSBW and inferred lateral diffusivities in the

517 range 50-200 $\text{m}^2 \text{s}^{-1}$. In the smaller-amplitude BSBW intrusions, κ_H is expected to be lower. This
518 suggests that processes in addition to thermohaline intrusion fluxes, such as stirring by eddies, are
519 required to explain the value for lateral diffusivity in the BSBW.

520 The values inferred for κ_H may be used to estimate the approximate time required for a
521 temperature anomaly to diffuse across the basin. A diffusivity of $\kappa_H = 400 \pm 88 \text{ m}^2 \text{ s}^{-1}$ on
522 $\sigma = 28.01 \text{ kg m}^{-3}$ in the BSBW is associated with a rate of transport of 0.16-0.24 cm s^{-1} , where
523 κ_H is divided by the length scale associated with the centered difference used to calculate spa-
524 tial gradients (200 km - twice the 100 km grid spacing length scale). At this rate, a temperature
525 anomaly would be transported across the ~ 600 km wide deep basin in 8-12 years. This is in
526 rough agreement with the hydrographic observations, which show cold anomalies crossing the
527 deep Basin in about 10-12 years. McLaughlin et al. (2009) estimated a similar net rate of trans-
528 port for the warm FSBW temperature anomaly of 0.1-0.5 cm s^{-1} , which they associated with the
529 combined effects of the gyre and thermohaline intrusions. In the DTML, values for diffusivity are
530 lower than, but comparable to, those in the BSBW, in approximate agreement with hydrographic
531 profile data that show warm anomalies crossing the deep basin in about 8-12 years.

532 We caution that the results of the inverse method in the DTML may be inaccurate due to the
533 influence of enhanced vertical mixing in the southern basin near the margins and on the slope,
534 transport by the poorly resolved cyclonic boundary current, or both. (The assumption that vertical
535 mixing can be neglected in the BSBW appears valid.) Recall that the sign of the second EOF mode
536 in the DTML is opposite that in the FSBW, reflecting a warm anomaly in the southern basin, and
537 resulting in the (potentially incorrect) prediction of cyclonic Beaufort Gyre flow. Although the
538 exact heat budget of the DTML remains an open question, the available evidence from the EOF
539 analysis and the inverse method both suggest that along-isopycnal diffusion of heat into the basin
540 interior from the margins in the west and south is the most important factor.

541 While we have provided an alternate method of calculating lateral velocity and diffusivity, tighter
542 constraints are needed on estimates of these quantities in the deep Canada Basin. Future studies
543 might involve tracer release experiments, more extensive velocity measurements, or additional
544 hydrographic data and mixing measurements (particularly near the basin margins), any of which
545 would improve our understanding of the deep water masses. These deep water masses, which
546 represent a significant fraction of the water column in the Canada Basin, provide a record of the
547 evolution of the source waters and are an important component of the full Arctic Ocean heat and
548 freshwater budgets.

549 *Acknowledgments.* The data were collected and made available by the Beaufort Gyre Exploration
550 Program based at the Woods Hole Oceanographic Institution (<http://www.whoi.edu/beaufortgyre>)
551 in collaboration with researchers from Fisheries and Oceans Canada at the Institute of Ocean
552 Sciences. Funding was provided by the National Science Foundation Division of Polar Programs
553 under Award Number 1350046.

554 APPENDIX

555 **Appendix - EOF formalism**

556 Potential temperature data are arranged into an $m \times n$ matrix $A_\theta(\vec{x}, z)$, for n isopycnals sampled at
557 m hydrographic stations, and the mean potential temperature on each isopycnal, $\mu_{\theta n}$, is subtracted
558 from each data point on that isopycnal (column means are removed), so that

$$\tilde{A}_{\theta n} = A_{\theta n} - \mu_{\theta n}.$$

559 To prevent the results from being biased towards spatial patterns in the FSBW, which has lateral
560 variations an order of magnitude or more larger than those in the DTML, we divide the data on

561 each isopycnal by the standard deviation of measurements on that isopycnal, $\sigma_{\theta n}$, to give

$$X_{\theta n} = \tilde{A}_{\theta n} / \sigma_{\theta n}.$$

562 The result is a matrix X_{θ} of potential temperatures on isopycnal surfaces spanning the FSBW,
563 BSBW, and DTML, with zero mean and unit standard deviation.

564 EOF modes are determined using singular value decomposition, which produces ordered or-
565 thonormal modes, with the first mode capturing the most variance in the data. That is,

$$X_{\theta} = USV' = EOF(\vec{x}) PC(z),$$

566 where the matrix U provides the spatial patterns for each EOF mode (the columns of U are the spa-
567 tial EOFs), equivalent to the eigenvectors of the covariance matrix for X_{θ} . The diagonal elements
568 of S provide the associated eigenvalues when squared and divided by the sample size. The columns
569 of the matrix V provide the vertical structure of each EOF mode, and the principal components are
570 calculated from $PC = SV'$ (Figure 4).

571 The principal components can be related to the variance explained by each EOF mode on each
572 isopycnal as follows: $(PC^M / \sqrt{m-1})^2$, where PC^M is the principal component for the M th mode.
573 This is equivalent to calculating the r^2 -value for the correlation between that EOF mode and the
574 potential temperature field on each isopycnal (Figure 6).

575 To determine the sensitivity of the EOF results to spatial sampling and station locations, the data
576 are sub-sampled by selecting random combinations of stations and correlating the resulting EOF
577 modes to the original modes. Eliminating up to half of the original stations results in correlations
578 above $r = 0.9$ for the first two modes, indicating very low sensitivity. EOF analysis is not affected
579 by redundancy in the data; it does not require that measurements on successive isopycnals or
580 between adjacent stations be independent.

581 EOF modes and the associated principal components are non-dimensional, and can be difficult
582 to interpret in relation to the observations. The original data matrix is reconstructed as:

$$A_{\theta}(\vec{x}, z) = USV' \sigma_{\theta}(z) + \mu_{\theta}(z),$$

583 where σ_{θ} and μ_{θ} are vectors for the standard deviation and mean of the potential temperature,
584 respectively, on each isopycnal. A reconstruction of the potential temperature field can be ac-
585 complished using only a set number of modes. For example, a mode 1 reconstruction is given
586 by:

$$A_{\theta}^{M1} = U_{m1} S_{11} V'_{n1} \sigma_{\theta n} + \mu_{\theta n}.$$

587 The resulting $m \times n$ matrix provides the information in the original potential temperature field that
588 is captured by the first EOF mode on each isopycnal at each station. As such, the reconstructed
589 field has the same spatial pattern as the first EOF mode, but provides dimensional values.

590 **References**

- 591 Armitage, T. W. K., S. Bacon, A. L. Ridout, A. A. Petty, S. Wolbach, and M. Tsamados, 2017:
592 Arctic Ocean surface geostrophic circulation 2003–2014. *The Cryosphere*, **11** (4), 1767–1780,
593 doi:10.5194/tc-11-1767-2017.
- 594 Bebieva, Y., and M.-L. Timmermans, 2016: An examination of double-diffusive processes in a
595 mesoscale eddy in the Arctic Ocean. *Journal of Geophysical Research: Oceans*, **121** (1), 457–
596 475, doi:10.1002/2015JC011105.
- 597 Carmack, E., K. Aagaard, S. JH, P. RG, M. FA, M. RW, and J. EP, 1998: Thermohaline Transi-
598 tions. *Physical Processes in Lakes and Oceans*, J. Imberger, Ed., American Geophysical Union,
599 Washington, DC, chap. 12, 179–186.

600 Carmack, E. C., R. W. Macdonald, R. G. Perkin, F. A. McLaughlin, and R. J. Pearson, 1995:
601 Evidence for warming of atlantic water in the southern canadian basin of the arctic ocean:
602 Results from the larsen-93 expedition. *Geophysical Research Letters*, **22 (9)**, 1061–1064, doi:
603 10.1029/95GL00808.

604 Carmack, E. C., W. J. Williams, S. L. Zimmermann, and F. A. McLaughlin, 2012: The Arctic
605 Ocean warms from below. *Geophysical Research Letters*, **39 (7)**, doi:10.1029/2012GL050890.

606 Cole, S. T., C. Wortham, E. Kunze, and W. B. Owens, 2015: Eddy stirring and horizontal diffu-
607 sivity from Argo float observations: Geographic and depth variability. *Geophysical Research*
608 *Letters*, **42 (10)**, 3989–3997, doi:10.1002/2015GL063827.

609 Dosser, H. V., and L. Rainville, 2016: Dynamics of the changing near-inertial internal wave field
610 in the Arctic ocean. *Journal of Physical Oceanography*, **46 (2)**, doi:10.1175/JPO-D-15-0056.1.

611 Gavart, M., and P. De Mey, 1997: Isopycnal EOFs in the Azores Current Region: A Statistical
612 Tool for Dynamical Analysis and Data Assimilation. *Journal of Physical Oceanography*, doi:
613 10.1175/1520-0485(0)027<2146:IEITAC>2.0.CO;2.

614 Guthrie, J. D., J. H. Morison, and I. Fer, 2013: Revisiting internal waves and mixing in the Arctic
615 Ocean. *Journal of Geophysical Research: Oceans*, **118 (August)**, 3966–3977, doi:10.1002/jgrc.
616 20294.

617 Hughes, C. W., and P. D. Killworth, 1995: Effects of Bottom Topography in the Large-Scale
618 Circulation of the Southern Ocean. *Journal of Physical Oceanography*, **25**, 2485–2497.

619 Jakobsson, M., and Coauthors, 2012: The International Bathymetric Chart of the Arctic Ocean
620 (IBCAO) Version 3.0. *Geophysical Research Letters*, **39 (12)**, doi:10.1029/2012GL052219.

- 621 Killworth, P. D., 1986: A Bernoulli Inverse Method for Determining the Ocean Circulation. *Journal of Physical Oceanography*, **16** (12), 2031–2051, doi:10.1175/1520-0485(1986)016<2031:
622 ABIMFD>2.0.CO;2.
- 624 Lee, J. H., and G. Veronis, 1991: On the difference between tracer and geostrophic velocities obtained from C-SALT data. *Deep Sea Research Part A. Oceanographic Research Papers*, **38** (5),
625 555–568, doi:10.1016/0198-0149(91)90063-L.
- 627 Macdonald, R., E. Carmack, and D. Wallace, 1993: Tritium and radiocarbon dating of Canada
628 basin deep waters. *Science*, **259**, 103–104.
- 629 McLaughlin, F. A., E. C. Carmack, W. J. Williams, S. Zimmermann, K. Shimada, and M. Itoh,
630 2009: Joint effects of boundary currents and thermohaline intrusions on the warming of Atlantic
631 water in the Canada Basin, 1993–2007. *Journal of Geophysical Research-Oceans*, **114**, doi:
632 10.1029/2008jc005001.
- 633 McPhee, M. G., 2013: Intensification of Geostrophic Currents in the Canada Basin, Arctic Ocean.
634 *Journal of Climate*, **26** (10), 3130–3138, doi:10.1175/JCLI-D-12-00289.1.
- 635 Meneghello, G., J. Marshall, S. Cole, and M.-L. Timmermans, 2017: Observational inferences of
636 lateral eddy diffusivity in the halocline of the Beaufort Gyre. *Submitted to Geophysical Research
637 Letters*.
- 638 Newton, J. L., and L. K. Coachman, 1974: Atlantic Water Circulation in the Canada Basin. *ARCTIC
639 TIC*, **27** (4), 297–303.
- 640 Proshutinsky, A., and Coauthors, 2009: Beaufort Gyre freshwater reservoir: State and variability
641 from observations. *Journal of Geophysical Research-Oceans*, **114**, doi:10.1029/2008jc005104.

642 Rainville, L., and P. Winsor, 2008: Mixing across the Arctic ocean: Microstructure observa-
643 tions during the Beringia 2005 expedition. *Geophysical Research Letters*, **35**, doi:10.1029/
644 2008gl033532.

645 Rudels, B., E. P. Jones, U. Schauer, and P. Eriksson, 2004: Atlantic sources of the Arctic Ocean
646 surface and halocline waters. *Polar Research*, **23** (2), 181–208, doi:10.1111/j.1751-8369.2004.
647 tb00007.x.

648 Rudels, B., R. D. Muench, J. Gunn, U. Schauer, and H. J. Friedrich, 2000: Evolution of the arctic
649 ocean boundary current north of the siberian shelves. *Journal of Marine Systems*, **25** (1), 77 –
650 99, doi:https://doi.org/10.1016/S0924-7963(00)00009-9.

651 Spall, M. A., 2013: On the circulation of atlantic water in the arctic ocean. *Journal of Physical*
652 *Oceanography*, **43** (11), 2352–2371, doi:10.1175/JPO-D-13-079.1.

653 Stommel, H., and F. Schott, 1977: The Beta Spiral and the Determination of the Absolute Velocity
654 Field from Hydrographic Station Data. *Deep Sea Research*, **24**, 325–329.

655 Timmermans, M.-L., and C. Garrett, 2006: Evolution of the deep water in the canadian basin in
656 the arctic ocean. *Journal of Physical Oceanography*, **36** (5), 866–874, doi:10.1175/JPO2906.1.

657 Timmermans, M.-L., C. Garrett, and E. Carmack, 2003: The Thermohaline Structure and Evolu-
658 tion of the Deep Water in the Canada Basin, Arctic Ocean. *Deep Sea Research Part I: Oceano-*
659 *graphic Research Papers*, **50**.

660 Timmermans, M.-L., J. Toole, R. Krishfield, and P. Winsor, 2008: Ice-Tethered Profiler observa-
661 tions of the double-diffusive staircase in the Canada Basin thermocline. *Journal of Geophysical*
662 *Research*, **113**, 1–10, doi:10.1029/2008JC004829.

- 663 Timmermans, M.-L., P. Winsor, and J. A. Whitehead, 2005: Deep-Water Flow over the
664 Lomonosov Ridge in the Arctic Ocean. *Journal of Physical Oceanography*, **35** (8), 1489–1493,
665 doi:10.1175/JPO2765.1.
- 666 Walsh, D., and E. Carmack, 2002: A note on evanescent behavior of Arctic thermohaline intru-
667 sions. *Journal of Marine Research*, **60**, 281–310.
- 668 Walsh, D., and E. Carmack, 2003: The nested structure of Arctic thermohaline intrusions. *Ocean*
669 *Modelling*, **5**, 267–289, doi:10.1016/s1463-5003(02)00056-2.
- 670 Woodgate, R. A., K. Aagaard, J. H. Swift, W. M. Smethie, and K. K. Falkner, 2007: Atlantic water
671 circulation over the Mendeleev Ridge and Chukchi Borderland from thermohaline intrusions
672 and water mass properties. *Journal of Geophysical Research: Oceans*, **112** (C2), doi:10.1029/
673 2005JC003416.
- 674 Zhao, M., M.-L. Timmermans, S. Cole, R. Krishfield, and J. Toole, 2016: Evolution of the eddy
675 field in the Arctic Ocean’s Canada Basin, 2005–2015. *Geophysical Research Letters*, **43** (15),
676 8106–8114, doi:10.1002/2016GL069671.
- 677 Zika, J. D., T. J. McDougall, and B. M. Sloyan, 2010: A Tracer-Contour Inverse Method for
678 Estimating Ocean Circulation and Mixing. *Journal of Physical Oceanography*, **40** (1), 26–47,
679 doi:10.1175/2009JPO4208.1.

680 **LIST OF FIGURES**

681 **Fig. 1.** a) Map of Canada Basin showing typical hydrographic sampling pattern (from 2007). Con-
682 tours show ocean bottom depth, with land in black. b) Representative temperature-salinity
683 diagram from 140°W and 74°N (gold star on map) from 2004 (blue) and 2014 (red), with
684 isopycnals in gray. Water masses are labelled. Inset shows the DTML. c) Profiles of poten-
685 tial temperature from the same location. Inset shows the DTML and deep double-diffusive
686 staircase. 35

687 **Fig. 2.** Potential temperature θ , referenced to the surface, vs. salinity S from 140°W and 74°N (gold
688 star on map in Figure 1), with profiles from 2003 to 2015 colored by year. Inset shows the
689 DTML. Note that this general picture holds for all stations in the deep Canada Basin. Water
690 masses are labelled and the table below gives 2003 to 2015 trends in potential temperature
691 ($\partial_t \theta$) and salinity ($\partial_t S$) on specified isopycnals in the BSBW and the DTML determined
692 based on a linear fit to basin mean values for all profiles with ocean bottom depth >3000 m,
693 with standard error. 36

694 **Fig. 3.** Spatial maps of potential temperature referenced to the surface for the a) FSBW on $\sigma =$
695 27.925 kg m⁻³, b) BSBW on $\sigma = 28.010$ kg m⁻³, and c) DTML on $\sigma = 28.097$ kg m⁻³,
696 objectively mapped using all hydrographic data from 2003 to 2015. The temporal trend
697 about the mean has been removed before mapping. Regions further than 100 km from a
698 station location are masked out in white. Black circles are station locations. Gray contours
699 are the 500 m to 3500 m isobaths in increments of 1000 m. 37

700 **Fig. 4.** a) EOF mode 1 and mode 2 spatial patterns of potential temperature on isopycnals from
701 2004, normalized to unit standard deviation. Isopycnals are chosen to be spaced roughly
702 every 50 m in the vertical in the FSBW, BSBW, and DTML water masses. b) Total variance
703 in the data explained by each EOF mode, cut off at the 10th mode. Only the first 5 modes are
704 statistically distinguishable from noise. c) Principal components corresponding to the first
705 (red) and second (blue) EOF spatial modes, with normalized amplitudes that correspond to
706 a 1 standard deviation change in the EOF modes, as in a). The PCs are plotted as a function
707 of average isopycnal depth, alongside a typical potential temperature profile with an inset
708 showing the DTML. The approximate depth range for each water mass is indicated. 38

709 **Fig. 5.** a) Correlation coefficients for the EOF mode 1 spatial pattern for each year with every other
710 year, for potential temperature on isopycnals. Note that the colorscale begins at $r = 0.75$. b)
711 Spatial maps of the first EOF mode for 2004 and 2014 ($r = 0.95$), with the data averaged
712 onto a 4° longitude by 1° latitude grid, which allows the correlations to be performed despite
713 differences in precise station location from one year to the next. Only grid boxes with profile
714 data available for both years are included in a given correlation. 39

715 **Fig. 6.** a) Percentage of the variance in the data on each isopycnal explained by the first EOF mode,
716 for each year. The mode 1 spatial pattern for a given year captures a certain amount of the
717 variability in the observed potential temperature field on each isopycnal, which is quanti-
718 fied by converting the first PC to percent variance explained (Appendix). For example, the
719 column for 2004 is calculated from the first PC for 2004 (Figure 4c), and quantifies how
720 well the first EOF mode for 2004 (Figure 4a) captures variations in the observed potential
721 temperature field from 2004. b) The same, but for the second EOF mode. 40

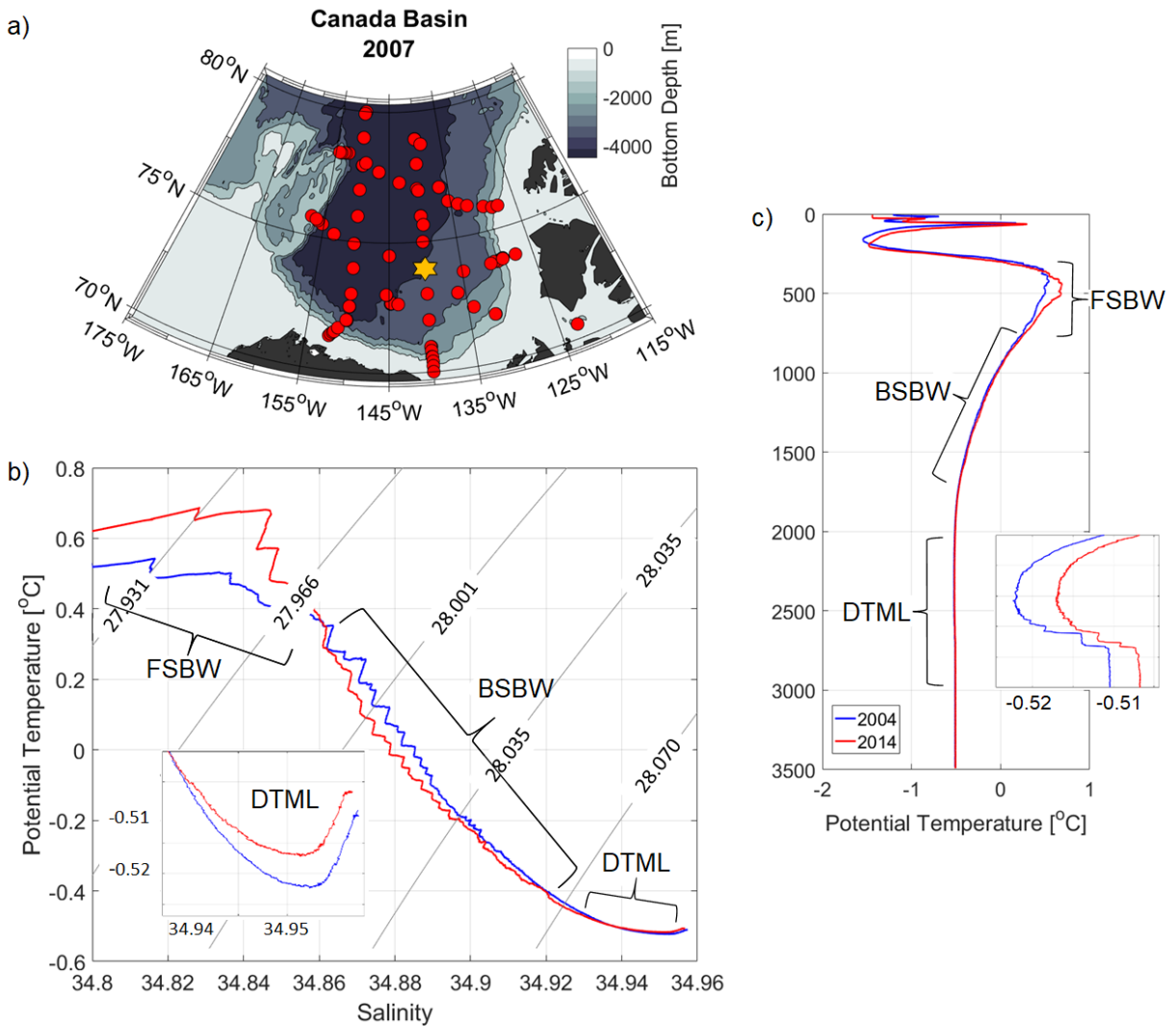
722 **Fig. 7.** a) Correlation coefficients for correlations between the first EOF mode for isopycnal depth
723 for each year from 2003 to 2015 with every other year. Note that the colorscale begins at
724 $r = 0.5$. To perform the correlations, data are gridded as in Figure 5. b) Grid-average of
725 the first EOF mode for isopycnal depth for every year from 2003 to 2015, for stations with

726 bottom depth >3000 m. The spatial pattern has been scaled to have standard deviation equal
 727 to one. Higher (more positive) values correspond to isopycnal depths further down in the
 728 water column. Light gray lines are the 500, 1500, 2500, and 3500 m isobaths. 41

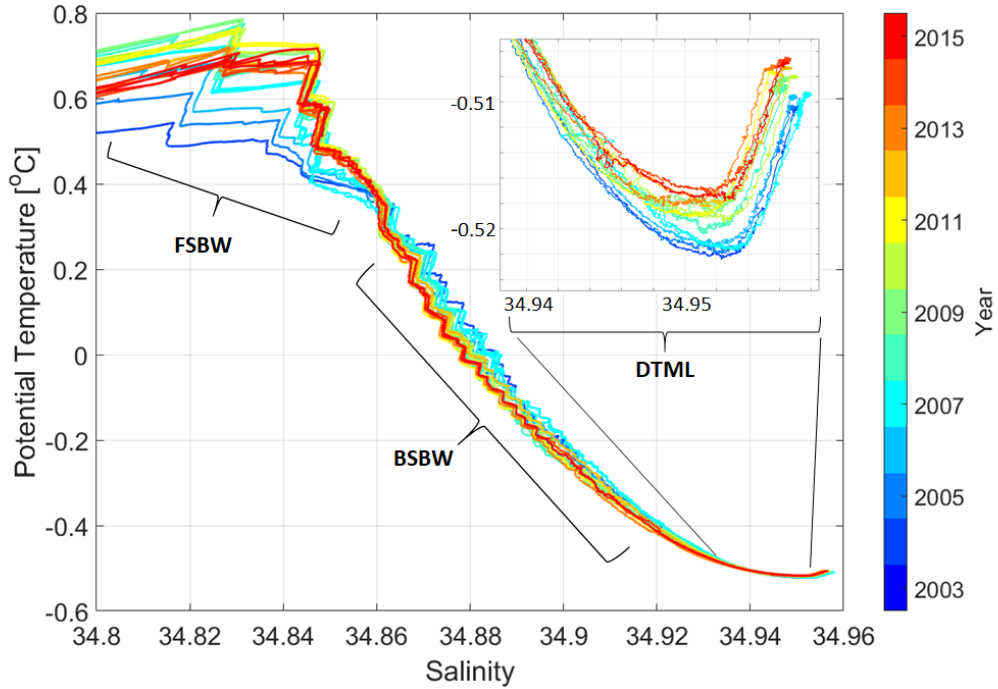
729 **Fig. 8.** a) Potential temperature of the DTML on $\sigma = 28.097 \text{ kg m}^{-3}$ in 2011. b) Potential tem-
 730 perature field on the same isopycnal reconstructed using only the first two EOF modes. The
 731 color scale is the same for both fields, and the temporal trend has not been removed from the
 732 reconstructed field, to allow a one-to-one comparison. Black lines are the 500, 1500, 2500,
 733 and 3500 m isobaths. 42

734 **Fig. 9.** a) Least-squares linear fit to data on $\sigma = 28.01 \text{ kg m}^{-3}$ (BSBW), for the advective, τ_1 ,
 735 and diffusive, τ_2 , terms in (4). Each point is the value from an individual grid box for the
 736 grid shown in Figure 7. b) Results for the estimated geostrophic Beaufort Gyre circulation
 737 on the same isopycnal, determined using the velocity magnitude calculated from the inverse
 738 method and velocity direction determined from the geostrophic streamfunction. Colors show
 739 the objectively mapped depth of the $\sigma = 28.01 \text{ kg m}^{-3}$ isopycnal. Geostrophic flow is
 740 assumed to follow depth contours of a given isopycnal. Light gray lines are the 500, 1500,
 741 2500, and 3500 m isobaths. 43

742 **Fig. 10.** DTML potential temperature on $\sigma = 28.097 \text{ kg m}^{-3}$, objectively mapped as in Figure 3,
 743 with black contours from -0.52 to -0.51°C in increments of 0.002°C , showing the roughly
 744 longitudinal variation across the central basin, and the influence of warming in the southern
 745 basin, near the margins, and on the slope. Red arrows show the assumed path of the bound-
 746 ary current, while blue spirals indicate regions with evidence of enhanced vertical mixing
 747 inferred from hydrographic profiles. Light gray lines are the 500, 1500, 2500, and 3500 m
 748 isobaths. 44

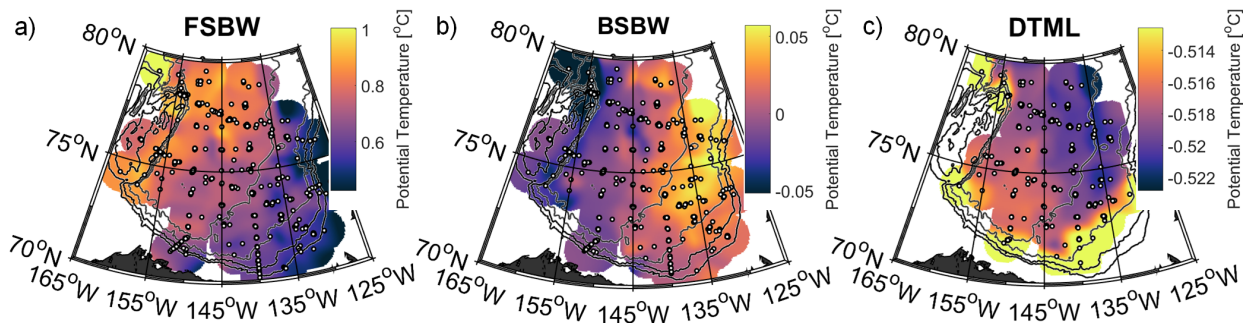


749 FIG. 1. a) Map of Canada Basin showing typical hydrographic sampling pattern (from 2007). Contours show
 750 ocean bottom depth, with land in black. b) Representative temperature-salinity diagram from 140°W and 74°N
 751 (gold star on map) from 2004 (blue) and 2014 (red), with isopycnals in gray. Water masses are labelled. Inset
 752 shows the DTML. c) Profiles of potential temperature from the same location. Inset shows the DTML and deep
 753 double-diffusive staircase.

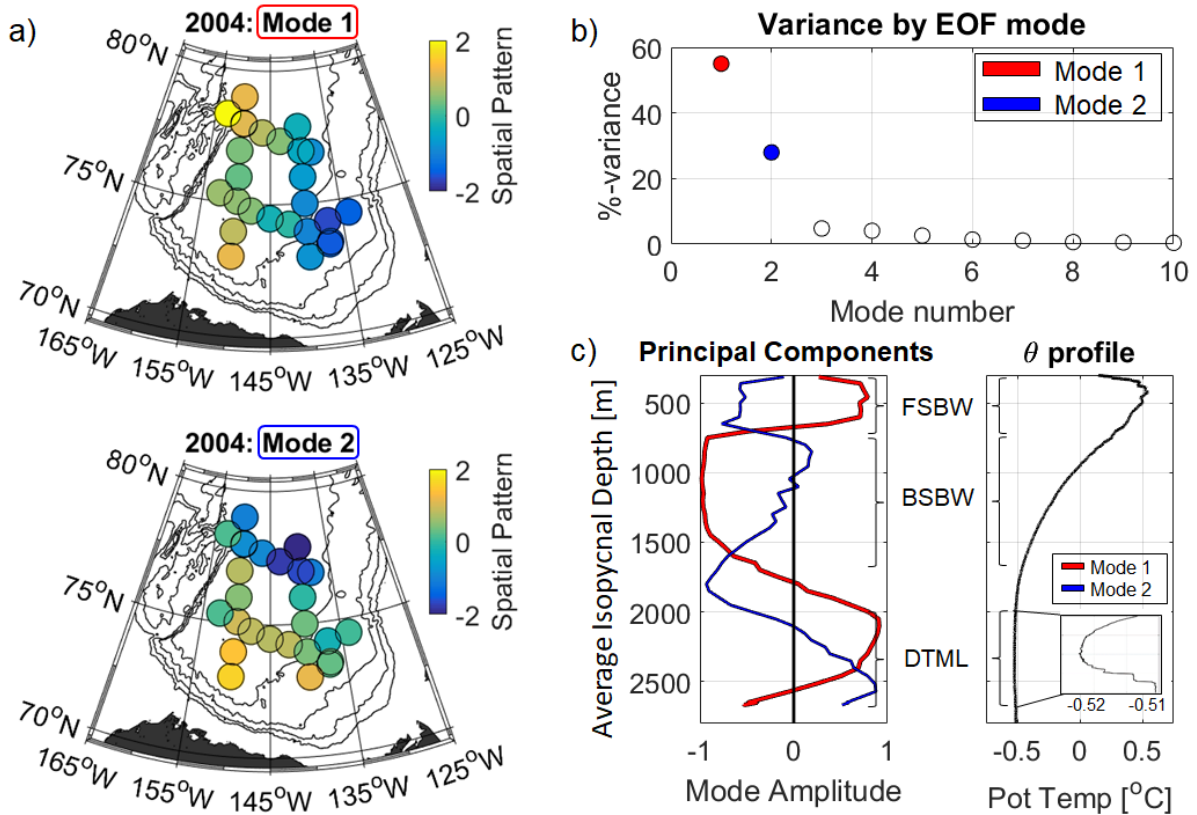


Linear trends in deep water mass properties		
	BSBW	DTML
	$\sigma = 28.010 \text{ kg m}^{-3}$	$\sigma = 28.097 \text{ kg m}^{-3}$
$\partial_t \theta$	$-2.8 \pm 0.3 \times 10^{-3} \text{ }^\circ\text{C yr}^{-1}$	$3.5 \pm 0.4 \times 10^{-4} \text{ }^\circ\text{C yr}^{-1}$
$\partial_t S$	$-1.9 \pm 0.2 \times 10^{-4} \text{ yr}^{-1}$	$2.2 \pm 0.3 \times 10^{-5} \text{ yr}^{-1}$

754 FIG. 2. Potential temperature θ , referenced to the surface, vs. salinity S from 140°W and 74°N (gold star
 755 on map in Figure 1), with profiles from 2003 to 2015 colored by year. Inset shows the DTML. Note that this
 756 general picture holds for all stations in the deep Canada Basin. Water masses are labelled and the table below
 757 gives 2003 to 2015 trends in potential temperature ($\partial_t \theta$) and salinity ($\partial_t S$) on specified isopycnals in the BSBW
 758 and the DTML determined based on a linear fit to basin mean values for all profiles with ocean bottom depth
 759 >3000 m, with standard error.

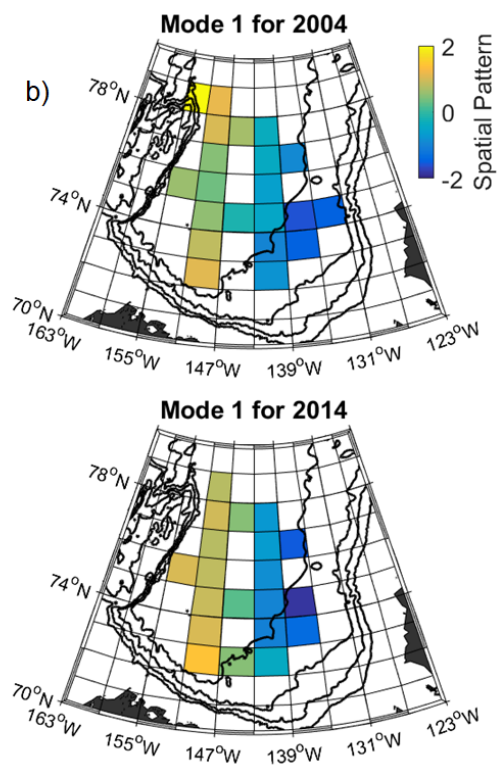
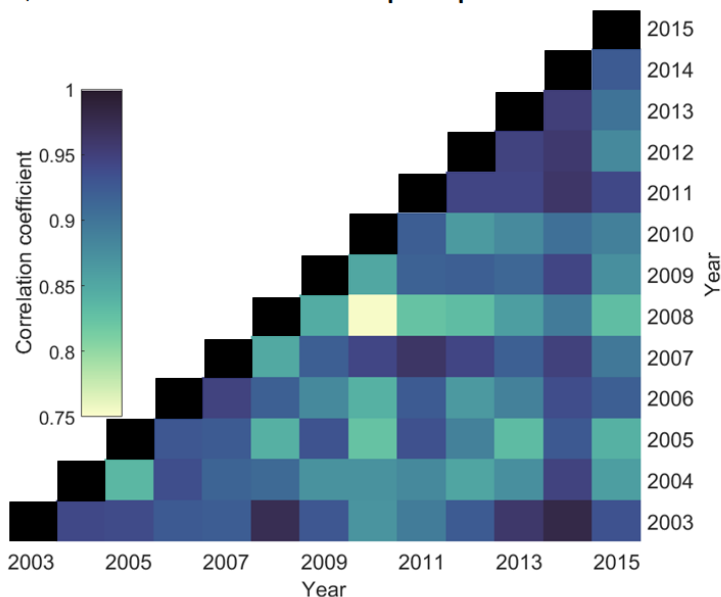


760 FIG. 3. Spatial maps of potential temperature referenced to the surface for the a) FSBW on $\sigma =$
 761 27.925 kg m^{-3} , b) BSBW on $\sigma = 28.010 \text{ kg m}^{-3}$, and c) DTML on $\sigma = 28.097 \text{ kg m}^{-3}$, objectively mapped
 762 using all hydrographic data from 2003 to 2015. The temporal trend about the mean has been removed before
 763 mapping. Regions further than 100 km from a station location are masked out in white. Black circles are station
 764 locations. Gray contours are the 500 m to 3500 m isobaths in increments of 1000 m.

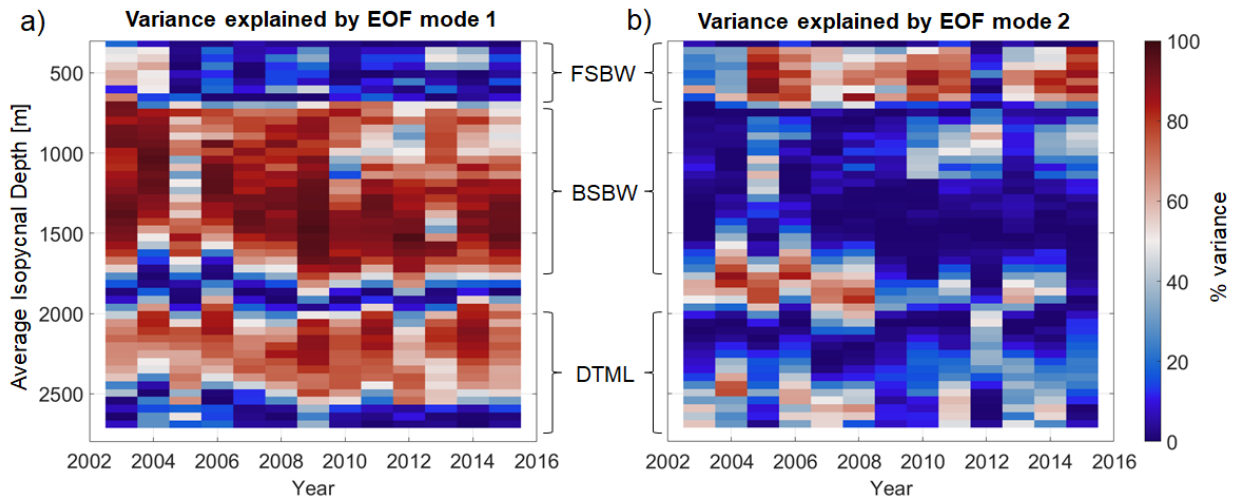


765 FIG. 4. a) EOF mode 1 and mode 2 spatial patterns of potential temperature on isopycnals from 2004, nor-
 766 malized to unit standard deviation. Isopycnals are chosen to be spaced roughly every 50 m in the vertical in
 767 the FSBW, BSBW, and DTML water masses. b) Total variance in the data explained by each EOF mode, cut
 768 off at the 10th mode. Only the first 5 modes are statistically distinguishable from noise. c) Principal compo-
 769 nents corresponding to the first (red) and second (blue) EOF spatial modes, with normalized amplitudes that
 770 correspond to a 1 standard deviation change in the EOF modes, as in a). The PCs are plotted as a function of
 771 average isopycnal depth, alongside a typical potential temperature profile with an inset showing the DTML. The
 772 approximate depth range for each water mass is indicated.

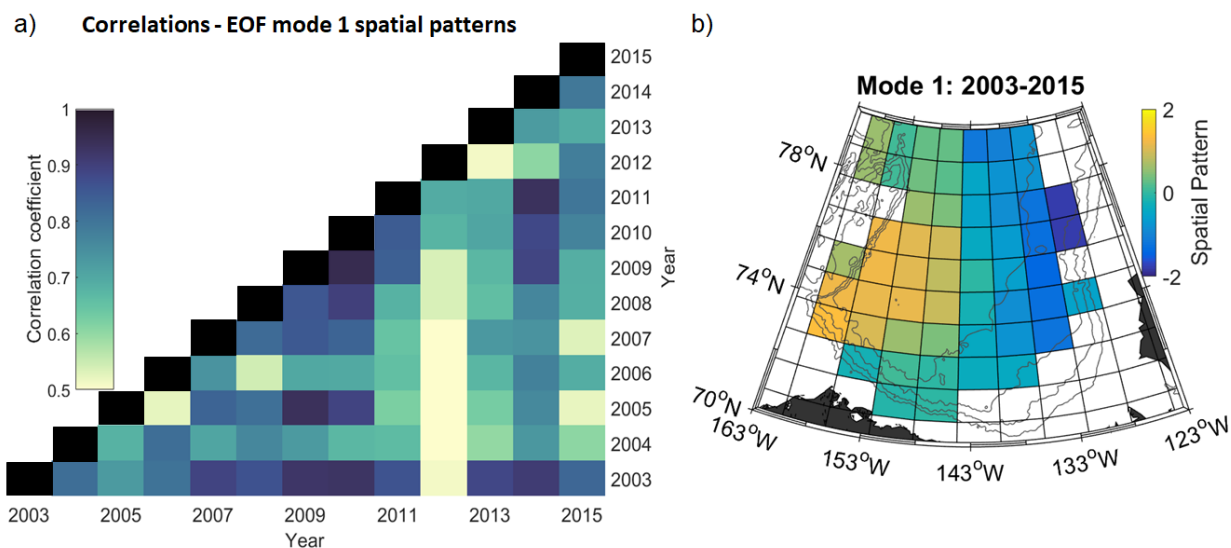
a) Correlations - EOF mode 1 spatial patterns



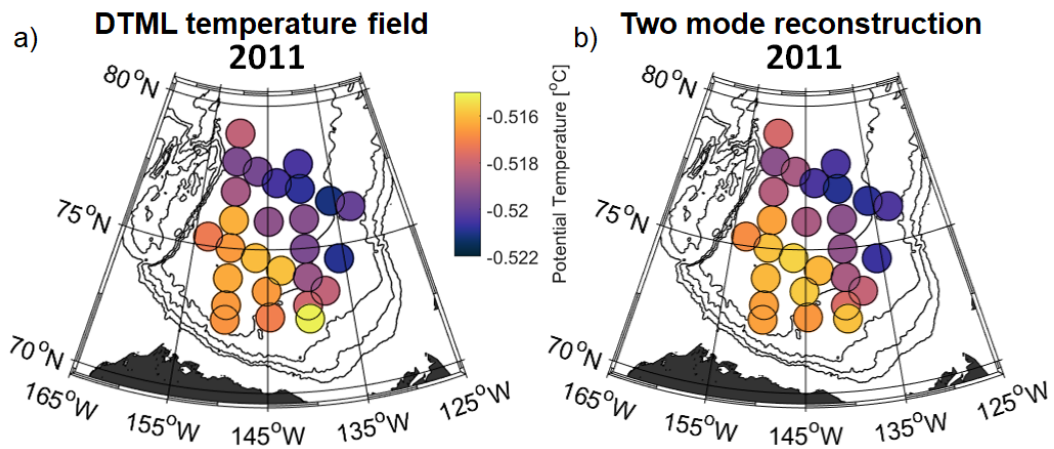
773 FIG. 5. a) Correlation coefficients for the EOF mode 1 spatial pattern for each year with every other year, for
 774 potential temperature on isopycnals. Note that the colorscale begins at $r = 0.75$. b) Spatial maps of the first EOF
 775 mode for 2004 and 2014 ($r = 0.95$), with the data averaged onto a 4° longitude by 1° latitude grid, which allows
 776 the correlations to be performed despite differences in precise station location from one year to the next. Only
 777 grid boxes with profile data available for both years are included in a given correlation.



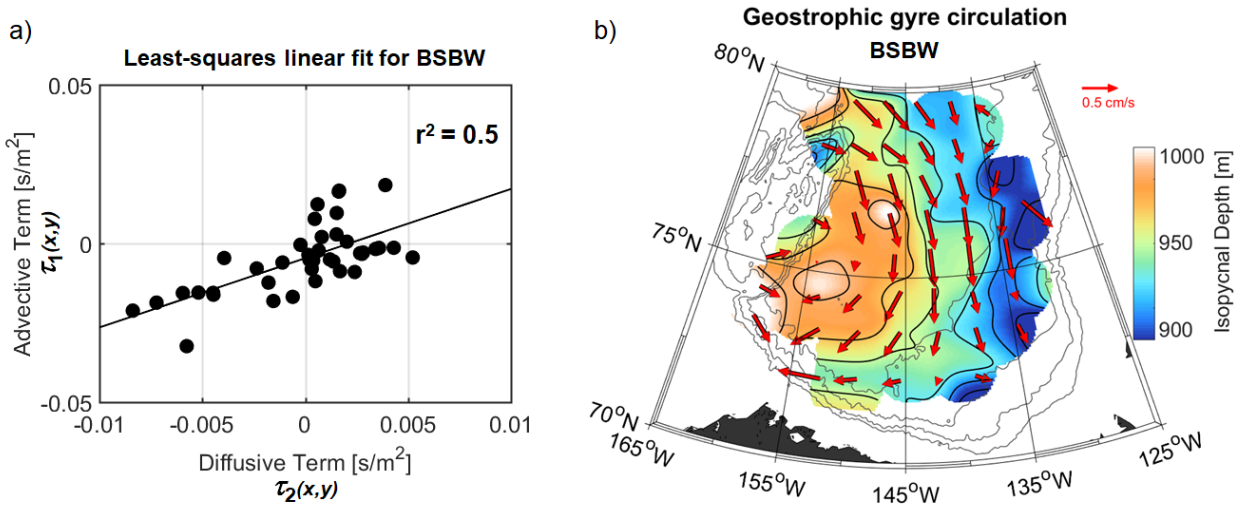
778 FIG. 6. a) Percentage of the variance in the data on each isopycnal explained by the first EOF mode, for each
 779 year. The mode 1 spatial pattern for a given year captures a certain amount of the variability in the observed
 780 potential temperature field on each isopycnal, which is quantified by converting the first PC to percent variance
 781 explained (Appendix). For example, the column for 2004 is calculated from the first PC for 2004 (Figure 4c),
 782 and quantifies how well the first EOF mode for 2004 (Figure 4a) captures variations in the observed potential
 783 temperature field from 2004. b) The same, but for the second EOF mode.



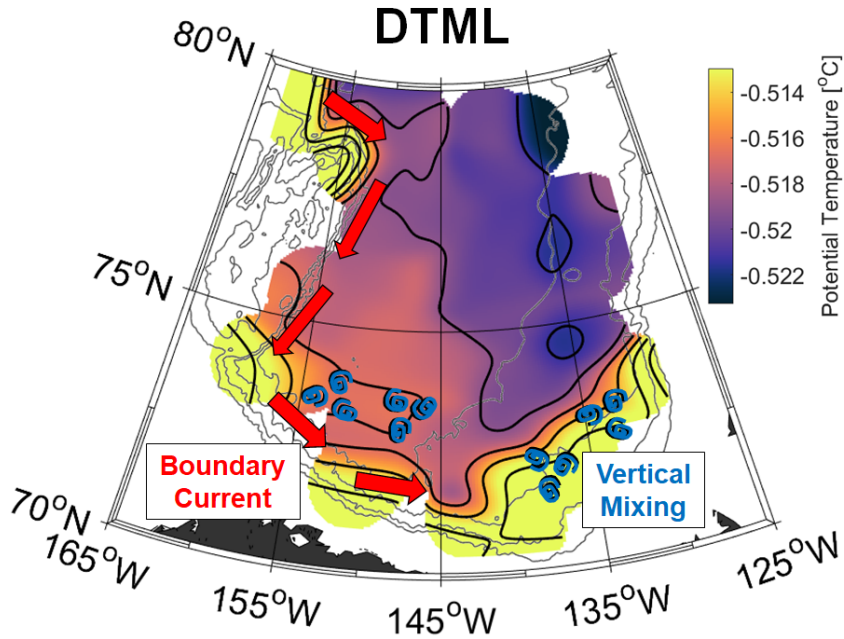
784 FIG. 7. a) Correlation coefficients for correlations between the first EOF mode for isopycnal depth for each
 785 year from 2003 to 2015 with every other year. Note that the colorscale begins at $r = 0.5$. To perform the
 786 correlations, data are gridded as in Figure 5. b) Grid-average of the first EOF mode for isopycnal depth for every
 787 year from 2003 to 2015, for stations with bottom depth >3000 m. The spatial pattern has been scaled to have
 788 standard deviation equal to one. Higher (more positive) values correspond to isopycnal depths further down in
 789 the water column. Light gray lines are the 500, 1500, 2500, and 3500 m isobaths.



790 FIG. 8. a) Potential temperature of the DTML on $\sigma = 28.097 \text{ kg m}^{-3}$ in 2011. b) Potential temperature
 791 field on the same isopycnal reconstructed using only the first two EOF modes. The color scale is the same for
 792 both fields, and the temporal trend has not been removed from the reconstructed field, to allow a one-to-one
 793 comparison. Black lines are the 500, 1500, 2500, and 3500 m isobaths.



794 FIG. 9. a) Least-squares linear fit to data on $\sigma = 28.01 \text{ kg m}^{-3}$ (BSBW), for the advective, τ_1 , and diffusive, τ_2 ,
 795 terms in (4). Each point is the value from an individual grid box for the grid shown in Figure 7. b) Results for the
 796 estimated geostrophic Beaufort Gyre circulation on the same isopycnal, determined using the velocity magnitude
 797 calculated from the inverse method and velocity direction determined from the geostrophic streamfunction.
 798 Colors show the objectively mapped depth of the $\sigma = 28.01 \text{ kg m}^{-3}$ isopycnal. Geostrophic flow is assumed to
 799 follow depth contours of a given isopycnal. Light gray lines are the 500, 1500, 2500, and 3500 m isobaths.



800 FIG. 10. DTML potential temperature on $\sigma = 28.097 \text{ kg m}^{-3}$, objectively mapped as in Figure 3, with black
 801 contours from -0.52 to -0.51°C in increments of 0.002°C , showing the roughly longitudinal variation across the
 802 central basin, and the influence of warming in the southern basin, near the margins, and on the slope. Red arrows
 803 show the assumed path of the boundary current, while blue spirals indicate regions with evidence of enhanced
 804 vertical mixing inferred from hydrographic profiles. Light gray lines are the 500, 1500, 2500, and 3500 m
 805 isobaths.